2023-05-19

Multiscale stiffness of human emphysematous precision cut lung slices

ENGINEERING

Multiscale stiffness of human emphysematous precision cut lung slices

Jae Hun Kim[1,2]†, Niccole Schaible[2,3]†, Joseph K. Hall[1]†, Erzsébet Bartolák-Suki[1], Yuqing Deng[4], Jacob Herrmann[1,5], Adam Sonnenberg[1], Holger P. Behrsing[6], Kenneth R. Lutchen[1], Ramaswamy Krishnan[2,3]‡*, Béla Suki[1,2]‡*

Emphysema is a debilitating disease that remodels the lung leading to reduced tissue stiffness. Thus, understanding emphysema progression requires assessing lung stiffness at both the tissue and alveolar scales. Here, we introduce an approach to determine multiscale tissue stiffness and apply it to precision-cut lung slices (PCLS). First, we established a framework for measuring stiffness of thin, disk-like samples. We then designed a device to verify this concept and validated its measuring capabilities using known samples. Next, we compared healthy and emphysematous human PCLS and found that the latter was 50% softer. Through computational network modeling, we discovered that this reduced macroscopic tissue stiffness was due to both microscopic septal wall remodeling and structural deterioration. Lastly, through protein expression profiling, we identified a wide spectrum of enzymes that can drive septal wall remodeling, which, together with mechanical forces, lead to rupture and structural deterioration of the emphysematous lung parenchyma.

INTRODUCTION

Chronic obstructive pulmonary disease (COPD) is a public health emergency with rapidly increasing prevalence, morbidity, and mortality and now ranked among the leading causes of death worldwide (*1*). A major subtype of COPD is emphysema that is characterized by aberrant mechanotransduction (*2*), remodeling of the extracellular matrix (ECM) of the lung parenchyma (*3*, *4*), reduced organ-level tissue stiffness (*5*), and hindered gas exchange. The precise mechanisms linking microscale alveolar remodeling to macroscale tissue stiffness, however, remain speculative due primarily to difficulties in obtaining reliable data. Such difficulties stem from the heterogeneity of the lung structure including numerous air sacs, thin septal walls, conducting airways, and vessels, complex shape of the lung boundaries, and cyclic mechanical interactions between the chest wall and the lung during breathing, which together limit the accessibility of the cells and ECM in the deep regions of the lung to imaging.

Much of our current knowledge on lung stiffness and its biological consequences have been inferred from global measurements in intact respiratory systems (*6*, *7*) or direct measurements in excised whole lungs (*8*) or tissue strips (*9*, *10*) with alveoli preserved. A notable exception is the microscopic stiffness measurement obtained via atomic force microscopy (AFM) applied to lung strips attached to a stretchable membrane chip (*11*). However, this technique is limited to tiny regions of ultrathin lung sections (~20 μm) that does not adequately preserve the native shape of single alveoli. Another approach is to fit a nonlinear model to the stress-strain curve of lung tissue strips during uniaxial deformation (*12*). This analytical approach, however, neglects the heterogeneous three-dimensional (3D) structure and deformation of the lung parenchyma.

Here, we present a multiscale approach to measure lung tissue stiffness. First, we validated the approach using agarose gels of known stiffnesses. Next, we applied our approach to mouse and human precision cut lung slices (PCLS), including emphysematous tissues. We found that the emphysematous human PCLS (hPCLS) is ~50% softer than the healthy PCLS, and computational modeling revealed that this softening is associated with septal wall weakening and structural breakdown. Thus, we unveil a mechanistic link between macroscopic lung softening, structural deterioration, and loss of function due to reduced stiffness at the level of single septal walls in human emphysema. Lastly, we interpret these results with protein expression profiling which brings into focus possible molecular targets for future therapeutic interventions.

RESULTS

Concept of stiffness measurement

To establish the foundations for stiffness measurement, we first developed an axisymmetric finite element (FE) model in which a thin elastic sample with a range of stiffness and thickness values is attached to and radially stretched by a membrane (Fig. 1A). We assume that both the membrane and the sample follow linearly elastic behavior with a no-slip condition at their interface (Materials and Methods). When the membrane is radially stretched, the global radial strain of the membrane is given by

$$\varepsilon_{rr}^{o} = \Delta r_{memb} / r_{memb}^{o} \times 100 \quad (1)$$

where Δr_{memb} denotes the change of the radius, and r_{memb}^{o} is the stress-free radius. Following a stretch of the membrane without a sample to $\varepsilon_{rr}^{o} = 13\%$, the local radial strain ε_{rr} computed as the gradient of radial displacement at the top surface of the membrane is equal to the global strain ε_{rr}^{o} over all radial positions, which is expected for the case of a uniform equibiaxial stretch applied to a

[1]Department of Biomedical Engineering, Boston University, Boston, MA, USA. [2]Mechanobiologix, LLC, Newton, MA, USA. [3]Center for Vascular Biology Research, Department of Emergency Medicine, Beth Israel Deaconess Medical Center and Harvard Medical School, Boston, MA, USA. [4]Department of Mechanical Engineering, Boston University, Boston, MA, USA. [5]University of Iowa, Iowa City, IA, USA. [6]Institute for In Vitro Sciences, Gaithersburg, MD, USA.
*Corresponding author. Email: bsuki@bu.edu (B.S.); rkrishn2@bidmc.harvard.edu (R.K.)
†These authors contributed equally to this work.
‡These authors contributed equally to this work.

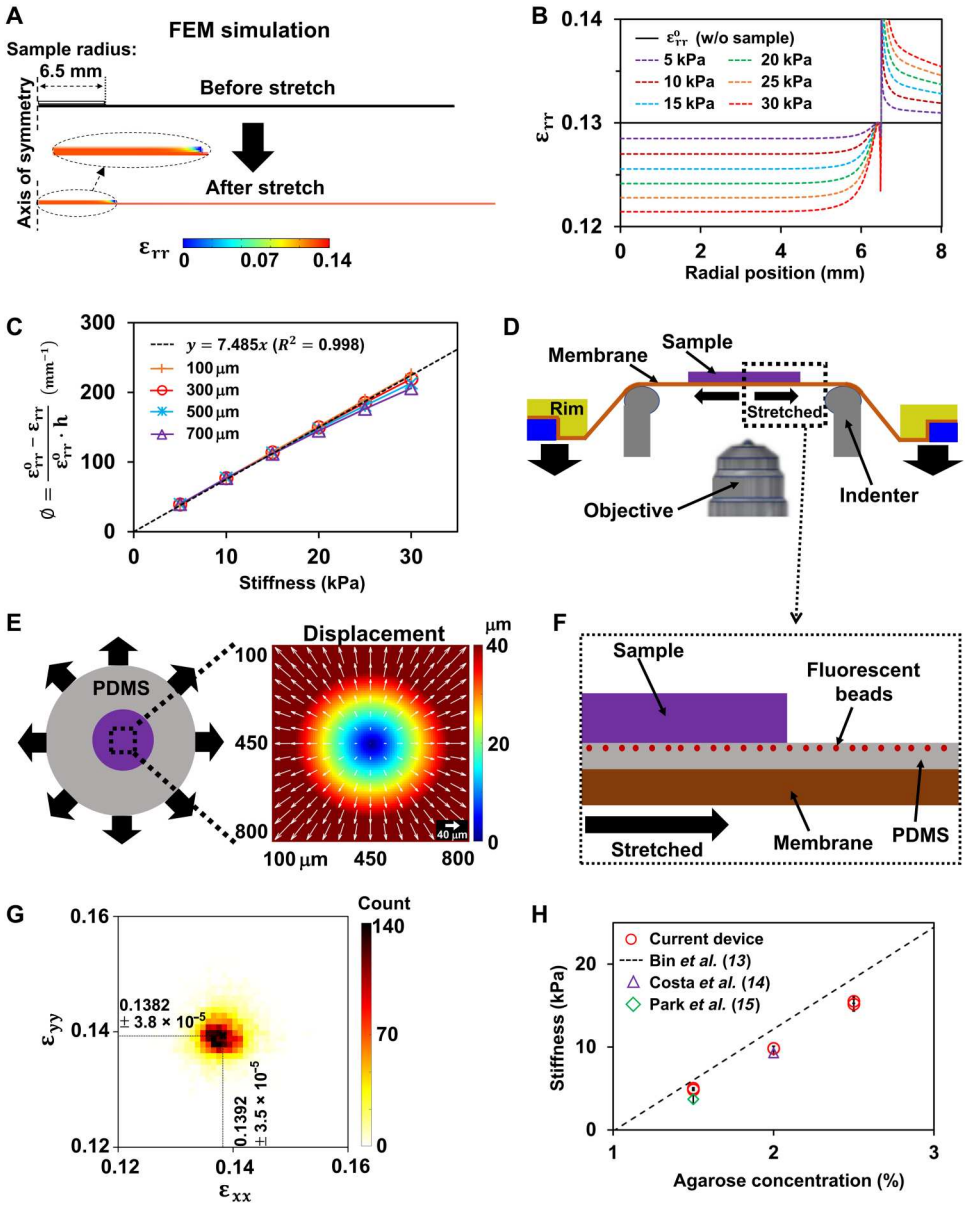

Fig. 1. Simulation and measurement of stiffness. (**A**) Axisymmetric FE model simulates stretching of a sample of 6.5-mm radius attached to a membrane of 38-mm radius. Color codes depict the radial normal strain, ε_{rr}. Inset: Zoomed in view of strain. (**B**) ε_{rr} versus radial position measured at the interface between the bottom of the sample and the membrane with varying sample stiffnesses. Black solid line represents the global strain without a sample, ε^o_{rr}. (**C**) The difference of strains ($\varepsilon^o_{rr} - \varepsilon_{rr}$) normalized with ε^o_{rr} and sample thickness *h* increases with increasing sample stiffness. Black dotted line depicts a linear regression across all simulations. (**D**) Schematic of the experimental setup. A membrane and an attached sample are biaxially stretched by the indenter. (**E**) Schematic of the membrane-sample system and a color-coded map of bead displacements overlaid with vectors (white) acquired near the center while being stretched without a sample. Scale arrow = 40 μm. (**F**) A zoomed side view of the membrane and the sample. The membrane is coated with a much softer PDMS layer, in which fluorescent beads are embedded at the top surface. (**G**) A histogram plot of strain components, ε_{xx} and ε_{yy}, computed from each pixel in (E). Dotted lines depict averages of all pixels. Numbers indicate average strains and SEs of ε_{xx} and ε_{yy}. (**H**) Stiffness of agarose samples measured using the current device (red). Dashed line and green and purple markers indicate the stiffnesses previously measured using the unconfined compression (*13*) and AFM (*14*, *15*), respectively.

homogeneous membrane (black line in Fig. 1B). However, when a sample is attached to the membrane, imposing the same global strain results in a nonhomogeneous strain field at the interface between the sample and the membrane (colored lines in Fig. 1B and fig. S1). Specifically, the local strain is smaller than ε^o_{rr} in the region under the sample (<6.5 mm) but larger than ε^o_{rr} outside the sample region (>6.5 mm). Moreover, ε_{rr} within the sample region is nearly constant up to ~3 mm of radial position regardless of sample stiffness or thickness (Fig. 1B and fig. S2A). The difference between ε^o_{rr} and ε_{rr} systematically increased with both the stiffness and thickness of the sample. When we normalize the relative

change in radial strain by the thickness h of the sample

$$\phi = \frac{\varepsilon_{rr}^{o} - \varepsilon_{rr}}{\varepsilon_{rr}^{o} h} \quad (2)$$

we find a single linear relationship between the ϕ and sample stiffness for all values of h (Fig. 1C). A linear regression over all cases provides thus a robust relationship between ϕ and stiffnesses (black dashed line in Fig. 1C; $r^2 = 0.999$). Furthermore, this relationship does not depend on the magnitude of the global strain ε_{rr}^{o} applied to the membrane-sample system (fig. S2B). This linear relationship establishes the basis for estimating the stiffness of an arbitrary sample by measuring strains near the center of a sample (radial position, <3 mm), while the membrane-sample system is stretched equibiaxially.

A novel device to deliver equibiaxial stretch

We implemented the concept of stiffness measurements by building a prototype device, which applies equibiaxial stretch to a membrane holding a sheet-like sample while simultaneously mapping the spatial distribution of displacements and strains underneath the sample (Fig. 1D and fig. S3). This is enabled by a custom-designed elastic composite substrate consisting of a stiff silicon membrane coated with a layer of soft polydimethylsiloxane (PDMS) gel (NuSil Silicone Technologies, Carpinteria, CA) with fluorescent beads embedded at the top surface (Fig. 1F) (Materials and Methods). Using an inverted microscope, the device allows imaging the fluorescent beads at the interface between the bottom of the sample and the membrane composite during stretch from below (Fig. 1D). In this manner, the composite acts as a displacement sensor.

Figure 1E depicts a representative 0.9 mm by 0.9 mm displacement map acquired near the center of the membrane while being biaxially stretched. Circular patterns in the displacement map and overlaid vectors (white) suggest that the displacements are radially symmetric. For additional clarity, we compiled Fig. 1G that depicts a histogram of normal strain components, ε_{xx} and ε_{yy}, computed from every pixel in the displacement map in Fig. 1E. The mean and the SE of ε_{xx} and ε_{yy} are $0.1383 \pm 3.8 \cdot 10^{-5}$ and $0.1392 \pm 3.9 \cdot 10^{-5}$, respectively. The narrow distributions (Fig. 1G) and nearly identical mean values of normal strain components ($\varepsilon_{xx}/\varepsilon_{yy} = 0.9928$) confirm that the device delivers an equibiaxial stretch.

Validation of stiffness measurement

To validate the theoretically predicted relationship between ϕ and sample stiffnesses, we used agarose samples with three different concentrations, 1.5, 2.0, and 2.5%. Each agarose sample was approximately 6.5 mm in radius and 250 to 750 μm thick when measured using confocal microscopy (Materials and Methods). Two agarose samples were considered per concentration. Sample stiffness was determined by imposing a global stretch of approximately 13.9% applied to the membrane (fig. S4). Agarose stiffness progressively increased with increasing concentration (Fig. 1H). The Young's modulus was 4.93 ± 0.1 kPa (mean ± SD), 9.84 ±0.01 kPa, and 15.34 ± 0.17 kPa for agarose concentration of 1.5, 2.0, and 2.5%, respectively (red in Fig. 1H). These moduli values agree well with the experimental relationships between agarose concentration and stiffness previously obtained in unconfined compression tests (*13*) (dashed line in Fig. 1H) and are close to or slightly higher than those previously measured using AFM [green and purple markers; 3.7 ± 0.6 kPa for 1.5% (*14*) and 9.3 ± 0.23 kPa for 2.0% (*15*)].

To further validate the applicability of our device to heterogeneous samples, we fabricated porous and nonporous PDMS samples (Materials and Methods) and measured their stiffnesses. In addition to stiffness, our measurements also provide a map of the spatial distribution of strains that is related to the structural heterogeneity of the sample. A representative map of the average strain $(\varepsilon_{xx} + \varepsilon_{yy})/2$ of a porous PDMS sample depicts local strain "hotspots" that correspond to pores trapped within the sample (arrows in fig. S5A) that are clearly visible in the phase-contrast image (arrows in fig. S5B). The Young's modulus was 2.66 ± 0.13 kPa (mean ± SD) and 3.28 ±0.11 kPa for the porous and nonporous PDMS, respectively (fig. S5C). These values agree well with measurements independently obtained using a uniaxial stretch device (Materials and Methods) (2.63 ± 0.04 and 3.05±0.03 kPa for the porous and nonporous PDMS, respectively). Porous PDMS samples were softer than nonporous samples in both measurements (14% for the current device and 18% for the uniaxial stretcher device).

Stiffness of mouse PCLS

The ability to measure the stiffness of biological tissues was tested in eight mouse PCLS (mPCLS) samples acquired from C57BL/6J wild-type mice (*16*). Their stiffness values ranged from 3 to 6 kPa (median = 3.91 kPa) (Fig. 2A). A representative map of the average strain $(\varepsilon_{xx} + \varepsilon_{yy})/2$ depicts strain heterogeneities with size scales extending below 100 μm in a mPCLS sample (dark spots in Fig. 2B). Although the median stiffness of mPCLSs was close to that of the agarose samples (median =4.93 kPa), the presence of dark spots in the strain map suggests that the strains are more heterogeneous in the mPCLS than in the agarose samples (fig. S4). The F-test revealed a 10 times greater variability of strains for the mPCLSs ($P < 0.00001$). These results suggest that the strain heterogeneity seen in the mPCLSs is related to the structure of the lung parenchyma. A representative image of autofluorescence from an mPCLS sample in Fig. 2C depicts 50 to 100 μm sized alveolar structures that is consistent with measurements reported previously (*17*–*19*). To quantify the spatial correlations in strain and structure, we computed the spatial autocorrelation function $C(r)$ as a function of the distance (r) between two points (Materials and Methods) both from the strain maps and autofluorescence images (*20*). In each case (Fig. 2, K and L), $C(r)$ decays over a hundred micrometers. The characteristic length ρ at which $C(\rho) = 0.5$ is 22 ± 10 μm in strain maps and 13 ± 1 μm in autofluorescence images, respectively, confirming the close association between strain and structural heterogeneity.

Comparison of stiffnesses of human healthy and emphysematous PCLS

To test whether our approach can detect disease-related stiffness changes, we compared eight human PCLS (hPCLS) samples acquired from a healthy donor with six hPCLSs obtained from a donor with severe COPD. The stiffness of healthy hPCLSs ranged from 1 to 7 kPa (median = 2.28 kPa) (Fig. 2D), while the emphysematous hPCLS ranged from 0.1 to 2 kPa (median = 0.96 kPa) (Fig. 2G), which were statistically different from those of the healthy hPCLS [analysis of variance (ANOVA), $P = 0.012$]. Individually, the stiffness of emphysematous hPCLS is approximately half of

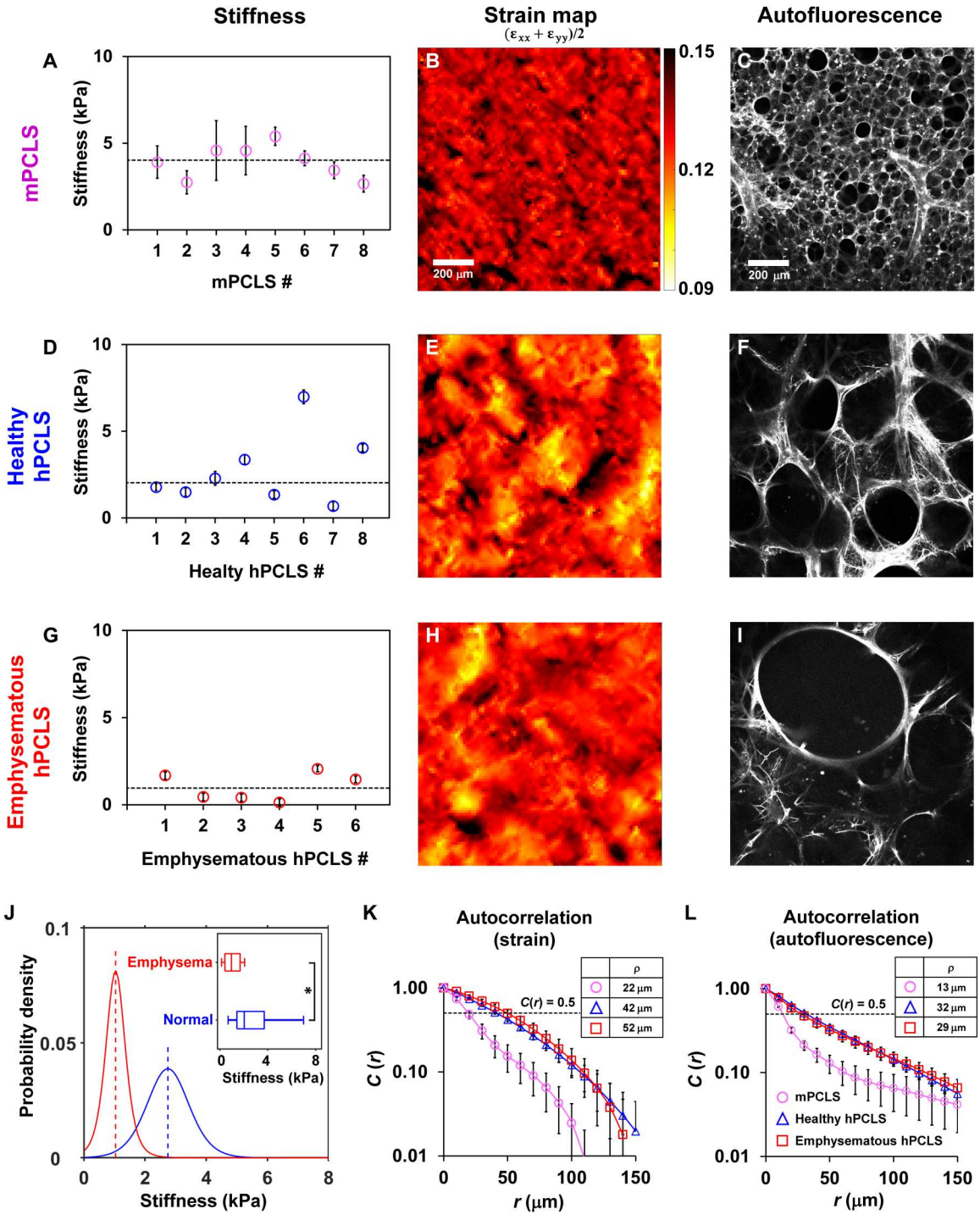

Fig. 2. Stiffness and correlation maps of mouse and hPCLS. (**A**) Stiffness of mPCLS is between 2 and 6 kPa (magenta markers). Dotted line indicates the median of all mPCLS (3.91 kPa). (**B**, **E**, and **H**) are color-coded maps of average strain, $(\varepsilon_{xx} + \varepsilon_{yy})/2$, measured in a mPCLS, a healthy hPCLS, and an emphysematous hPCLS, respectively. (**C**, **F**, and **I**) are autofluorescent images (from a different field of view) acquired from an mPCLS, a healthy hPCLS, and an emphysematous hPCLS, respectively. (**D**) Stiffness of a healthy PCLS ranges between 1 and 7 kPa (blue). Dotted line indicates the median (2.28 kPa). (**G**) Stiffness of an emphysematous PCLS is between 0.1 and 2 kPa. Dotted line indicates the median (0.96 kPa). (**J**) Bayesian estimation of the posterior distribution of stiffness of healthy and emphysematous hPCLS. Inset: Box plot comparing stiffness of healthy and emphysematous hPCLS shown in (D) and (G). *The stiffness of emphysematous hPCLS is significantly lower than that of the healthy hPCLS (one-tailed *t* test, $P = 0.026$; one-tailed Bayesian factor: 2.54). Boxplot shows medians and quartiles. Whiskers are maximum and minimum values. (**K**) Autocorrelation of strains acquired from mPCLS, healthy hPCLS, and emphysematous hPCLS group. A total of six to eight strain maps were analyzed for each group. (**L**) Autocorrelation of autofluorescence tissue images acquired from mPCLS, healthy hPCLS, and emphysematous hPCLS group. Sixteen images obtained from four tissues were used in each group. Error bars indicate SEs. On (K) and (L), the dotted lines indicate $C(\rho) = 0.5$, and the tables show ρ values at which $C(\rho) = 0.5$.

that of the healthy hPCLS (one-tailed *t* test, $P = 0.026$) (inset in Fig. 2J). To further compare the stiffness of healthy and emphysematous hPCLSs, we performed a Bayesian analysis of the mean stiffness (Fig. 2J) and its variance (fig. S6). The posterior distributions in Fig. 2J show little overlap between them with a one-sided Bayesian factor of 2.54.

Autofluorescence images show that the emphysematous sample (Fig. 2I) exhibited visually larger air spaces than the control sample (Fig. 2F) with air space sizes of ~200 μm, as previously reported (*21*). Unexpectedly, however, $C(r)$ of autofluorescence was not different between healthy and emphysematous hPCLSs (Fig. 2L; $\rho = 32 \pm 6$ and 29 ± 11 μm for healthy and emphysematous hPCLS, respectively; two-tailed *t* test, $P = 0.6$). Moreover, $C(r)$ of strain decayed similarly for both healthy and emphysematous hPCLS (Fig. 2K; ρ of strains: 42 ± 8 μm for healthy hPCLS and 52 ± 15 μm for emphysematous hPCLS; two-tailed *t* test, $P = 0.19$).

Network modeling to estimate local alveolar stiffness

The macroscopic stiffness of the PCLS depends on the constitutive properties of alveolar walls as well as the sizes of the alveoli. To estimate the average stiffness at a lower scale, namely, that of the alveolar septal walls, the size distribution of airspaces needs to be considered. Hence, we first analyzed the structure on both unfixed fluorescent (Fig. 2, F and I) and fixed histologic sections (fig. S13). A total of 183 and 209 alveoli were captured from the autofluorescent images (Fig. 3A) of healthy and emphysematous tissues, respectively. The area distributions of the healthy alveoli and the emphysematous alveoli (Fig. 3B) were found to be statistically significantly different (one-tailed Kolmogorov-Smirnov test, $P < 0.05$). Specifically, the emphysematous tissue alone displayed the likelihood of containing very large alveoli (far right of distribution curve). The equivalent alveolar diameters in the emphysematous tissue (249 ± 109 μm) were also significantly larger ($P < 0.05$) than in the healthy tissue (218 ± 67 μm). The wall thicknesses, with fixation shrinkage included, were 5.83 μm for the healthy tissue and 5.17 μm for the emphysematous tissue, which were significantly different ($P < 0.05$). Next, a set of network models with an area distribution identical to that of the healthy tissue were created, from which emphysematous networks were obtained by cutting springs (Fig. 3C). We found that the average number of springs that had to be cut from the healthy network to obtain the emphysematous network was $6.9 \pm 1.9\%$. Overall, 10 network pairs were created and tested. The elastic energy of the network pairs was computed as a function of strain on the entire network (Fig. 3D), which allowed us to estimate the Young's modulus of each network. The mean septal wall stiffness for the healthy tissue was 51.2 kPa and, for the emphysematous tissue, 25.7 kPa. Although this difference did not reach statistically significance ($P = 0.08$, Bayesian factor: 1.65) due to the large variability of individual values, a Bayesian analysis yielded posterior stiffness distributions with little overlap between the healthy and emphysematous cases (Fig. 3E).

Enzyme expressions and tissue deterioration in emphysema

To better understand what drives stiffness decline in emphysema, we first carried out protein profiling of the molecular weight distribution in the healthy and emphysematous hPCLSs by silver staining (fig. S15). Except for the lowest molecular weight range (~10 kDa), substantial differences were found between the healthy and emphysematous tissues with higher levels of protein species in the 200 to 250 kDa range and lower levels between 75 and 100 kDa in normal lung. It is noteworthy that soluble collagen is expressed at ~75 kDa. These differences were then further analyzed using a proteome profiler array for 35 human proteases, which screens for a wide spectrum of enzymes. The raw arrays for both the healthy and emphysematous subjects and the corresponding protein amounts are shown in Fig. 4 (A and B), respectively. The description of the full array is given in fig. S16. Many of the enzymes were significantly different between the healthy and emphysematous tissues. The full identification of the dots is given in fig. S16. Notably, three enzymes, Kallikrein 13, metalloproteinase (MMP)–10, and Urokinase, were only found in the emphysematous hPCLS. Next, we identified 13 enzymes (not including the above three enzymes) with amounts at least 1.5 times higher in the emphysematous than the healthy hPCLS (Fig. 4C). These enzyme expressions were associated with more inflammatory cells and identifiable sites of rupture in the emphysematous hPCLS.

DISCUSSION

We have introduced a novel approach to measure the stiffness of soft biological tissues and demonstrated that stiffness can be precisely estimated by applying equibiaxial stretch and tracking bead displacement at the membrane-sample interface. A key advantage of the approach is that it does not need a force sensor. With some caveats (note S1), this approach can be used to measure the stiffness of any soft material that can be adhered to the top surface of our membrane-gel system. We used agarose of different stiffnesses to validate the approach (Fig. 1H). As our primary tissue sample, we used the PCLS preparation that contains hundreds of alveoli and permits direct visualization of cellular and ECM changes in the native lung tissue (*16*, *22*–*24*). The PCLS has several practical advantages such as storage via cryopreservation (*16*, *25*), measurement of traction forces (*26*), widespread applicability to nearly every species including human, and suitability for high-resolution imaging as well as pharmacological and mechanical manipulations including responses to mechanical stretch (*27*–*30*) and neural stimulation (*31*, *32*). Comparing the stiffness of hPCLS from healthy and emphysematous subjects showed that tissue degradation leads to loss of function (Fig. 2J).

The changes in macroscopic stiffness (Fig. 2J) together with the fluorescent (Fig. 2, F and I) and histologic images (fig. S13A) provide a basis for assessing the loss of tissue function at the microscale. A network analysis of tissue structure and mechanics together with a microscale image analysis allowed us to quantify in the emphysematous hPCLS the partitioning of the loss of function at the macroscale between two sources: (i) structural alterations related to septal wall rupture (fig. S18) and (ii) reduced septal wall stiffness due to cellular remodeling. The results suggested that in addition to airspace enlargement, weakened septal walls substantially contribute to the decrease of macroscopic tissue level stiffness (Fig. 3E). However, these processes are not completely independent. Alveolar wall rupture—which can occur due to the mechanical forces of normal breathing in emphysema (*33*)—requires that inflammation-related (*34*) and enzyme-induced (*3*) remodeling of the septal wall lowers the failure stress of the collagen, elastin, and the entire alveolar wall (*35*). We observed that rupture was associated with local sites where inflammatory cells were also found (fig. S18).

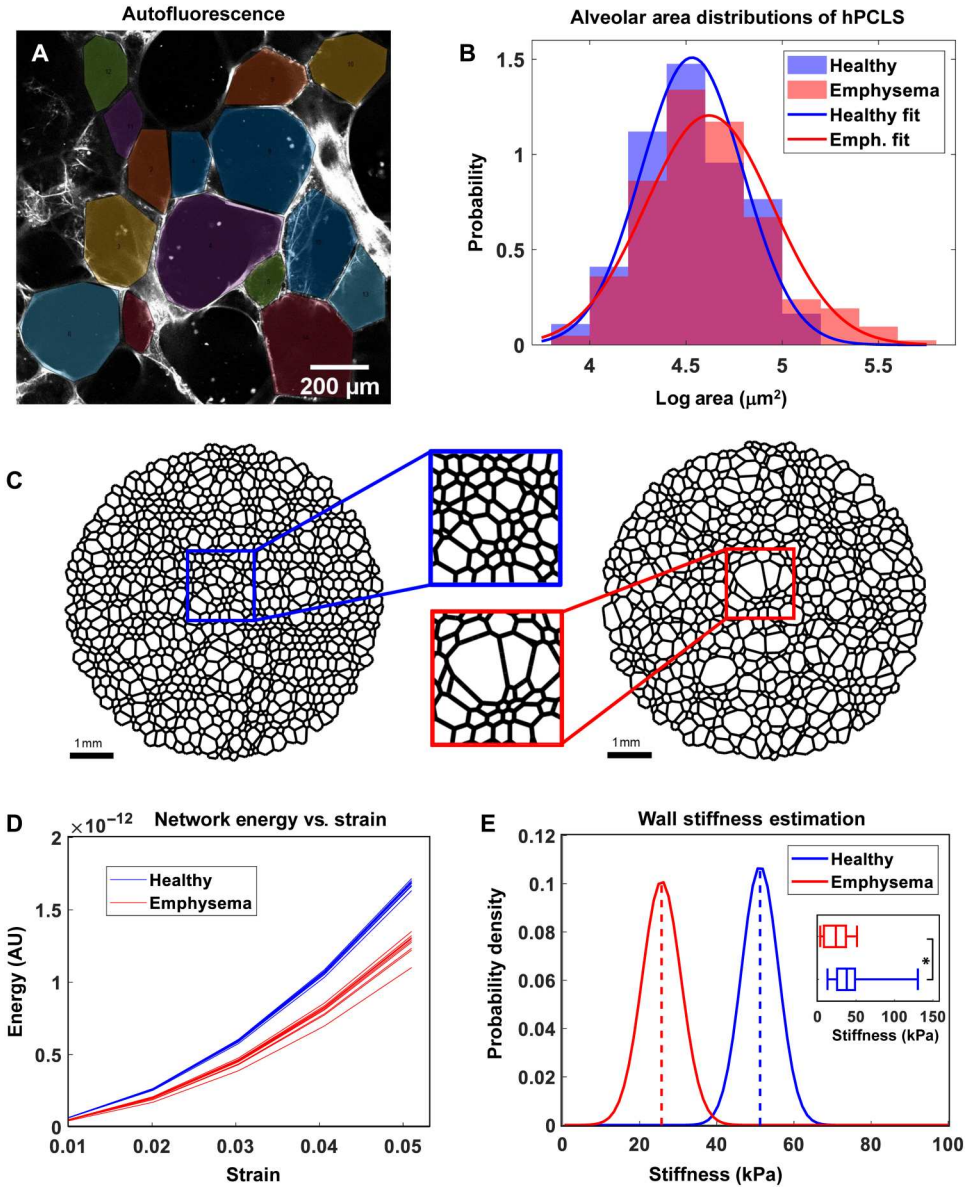

Fig. 3. Network modeling and stiffness estimation of hPCLS. (**A**) An example of color-coded alveolar airspaces identified from autofluorescent images taken from an hPCLS sample. (**B**) Comparison of the probability distributions of alveolar areas obtained from images similar to that in (A). The blue and red symbols denote measured distributions, and the corresponding solid lines are lognormal fits to the data obtained from healthy and emphysematous hPCLSs, respectively. (**C**) Spring network representations of hPCLS in 2D. Left shows a network of healthy hPCLS, and the right demonstrates airspace enlargement in an emphysematous hPCLS. The insets zoom into the square regions of each network. (**D**) Variation of strain energy with strain in 10 network pairs with area distributions pooled from the lognormal fits in (B). Blue and red curves correspond to networks representing healthy and emphysematous hPCLS, respectively. (**E**) Posterior distributions of the alveolar septal wall stiffness parameter for the networks representing healthy (blue) and emphysematous (red) hPCLS. Inset: Comparison of the means by *t* test ($P = 0.08$) and Bayesian analysis (Bayesian factor: 1.65). AU, arbitrary units.

The molecular level remodeling of the ECM of the septal wall is associated with an up-regulation of a wide spectrum of enzymes (Fig. 4B), a manifestation of biological complexity. Most of the enzymes that exhibited an expression at least 50% higher in emphysema such as a disintegrin and metalloprotease domain-8 (ADAM8) (*36*), ADAM9 (*37*), the cathepsins including B (*38*), E (*39*), L (*40*), and S (*41*) as well as all the MMPs (*42*–*44*) have been implicated in emphysema. While there seems to be no single biochemical signaling pathway that may account for their specific regulation, these enzymes participate in downstream processes, and many have the ability to cleave ECM molecules. This would suggest that enzyme activities eventually converge toward weakening of the walls with the inescapable end-result of mechanical force-induced rupture. These processes lead to deterioration of the normal structure and function of the lung parenchyma that is reflected in airspace enlargement and multiscale reduction in stiffness.

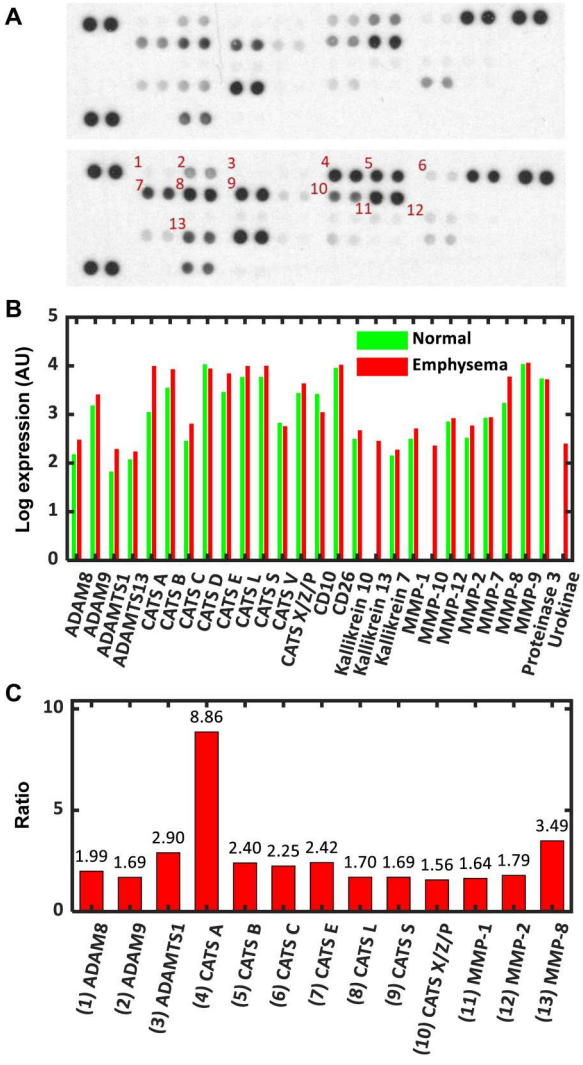

Fig. 4. Enzyme expressions in hPCLS. (**A**) Raw protein array images from the healthy (top) and emphysematous (bottom) hPCLSs. The darkness and size of the dots determine the relative quantities detected. Each enzyme is detected in duplicates. The red numbers refer to enzymes in (C). (**B**) Logarithm of the expression in arbitrary units of 27 enzymes included in the protein array. Those enzymes that had no detectable levels in both the healthy and emphysematous hPCLSs are not included. CATS denotes cathepsin. Notice that three enzymes, Kallikrein 13, MMP-10, and Urokinase, were not detectable in the healthy hPCLS. (**C**) Ratio of expressions of enzyme levels in the emphysematous and healthy hPCLSs for a subset of enzymes. Only those enzymes are included for which the level in emphysematous tissue is at least 1.5 times that in the healthy tissue. The numbers in front of the enzymes refer to the locations shown in red on (A) (bottom). The number above the bars are the actual ratios. Note that Kallikrein 13, MMP-10, and Urokinase are not included in the panel.

In conclusion, we have introduced a multiscale approach to measure lung tissue stiffness from the scale of many alveoli governing gas exchange to the scale of single septal walls where pathobiology drives disease progression. Using this approach, we have revealed a mechanistic link between macroscopic lung softening, microscopic structural deterioration, and loss of function in the human emphysematous lung parenchyma.

MATERIALS AND METHODS

Numerical computation

The computational foundation of the concept to measure stiffness was established by generating a 2D axisymmetric FE model using the COMSOL Multiphysics (version 4.3, COMSOL Inc.) software package. We first modeled the geometry of the device in which a composite membrane-sample system was indented by a hollow indenter (fig. S7A). We then modeled a simplified geometry in which a composite membrane-sample system was radially stretched (fig. S7B) and confirmed that the strain profiles from FE models with and without a hollow indenter were nearly identical far beyond the sample region (fig. S7C). Furthermore, $\varepsilon_{rr} = \varepsilon_{\theta\theta}$ and both strains were nearly constant within the sample region up to ~3 mm of radial position (fig. S3 and Fig. 1B). Thus, a composite of a Nusil layer and a silicone membrane was modeled as a single layer with an apparent composite modulus that was measured using the uniaxial stretcher device (see below), a thickness that was measured after assembly in the rim (Young′s modulus = 526 kPa, thickness = 140 μm) and Poisson′s ratio (ν) of 0.45. The sample was modeled as a layer with a diameter of 9 mm, Poisson′s ratio (ν) of 0.45, and various thicknesses (100 to 600 μm), and Young′s moduli (5 to 35 kPa). No slip between the sample and the composite membrane was allowed (see the "Adhesion of a sample to the membrane composite" section). For each simulation with a certain thickness and modulus of the sample, radial strain at the center of the interface between the sample and the composite membrane was computed as an output for the sample. To test the effect of sample shape and alignment on strain measurements, we also performed 3D FE modeling (fig. S8). 3D FE models with three cases, (i) a circular sample aligned at the center of a membrane, (ii) an elliptical sample aligned at the center of a membrane, and (iii) a circular sample aligned at 2 mm off from the center of the membrane, confirmed that the measured average strain $(\varepsilon_{xx} + \varepsilon_{yy})/2$ was not sensitive to sample shape or sample alignment relative to a membrane. All simulations were performed using a linear solver, MUMPS (Multifrontal Massively Parallel sparse direct Solver, COMSOL Multiphysics) with the nonlinear geometry option applied.

Device design

Figure 1D and fig. S3 are device schematics, comprising a custom well (light green in fig. S3), a hollow indenter (gray) fixed at the bottom of the well, and a rim assembly (yellow and blue) that can travel vertically. The vertical motion is controlled by a rotating fixture attached to the rim assembly. As the rim assembly travels downward, a membrane and an attached sample are biaxially stretched by the indenter (Fig. 1D). Note that the well is not displayed here. The deformation of the sample is imaged from below through an objective (10×). All parts constituting the stretching device were fabricated using polylactic acid filaments (MakerGear, Beachwood, OH) with the assistance of the Engineering Product Innovation Center at Boston University.

Preparation of a composite membrane

The composite membrane (Fig. 1F) consists of (i) a silicone membrane (Specialty Manufacturing Inc., Saginaw, MI) at the bottom, (ii) 0.5-μm yellow-green beads (F8813, Invitrogen), (iii) a soft PDMS elastomeric gel layer (*45*) (NuSil-8100; Silicone

Technologies, Carpinteria, CA) (Young's modulus = 3 kPa, thickness = 100 μm) in the middle, and (iv) a PDMS layer bearing 1-μm-diameter custom-synthesized red fluorescent beads (*45*, *46*) (Young's modulus = 3 kPa, thickness = 1 μm) at the top.

The fabrication proceeds as follows: (i) A section of the silicone membrane is stretched over a glass plate (110 mm by 78 mm by 1 mm) for support. The edges of the membrane are secured underneath the four corners of the glass plate with tape. Any trapped air pockets are eliminated by gentle rubbing so that the membrane becomes flush against the glass plate. (ii) Forty microliters of 0.5-μm-diameter yellow-green fluorescent beads was dispersed in 10 ml of Hanks' balanced salt solution (HBSS) and added to the top of the membrane-on-plate. The bead solution is allowed to air dry overnight. The membrane-on-plate is then rinsed with distilled water and air-dried leaving behind a layer of yellow-green beads deposited to the top of the membrane. (iii) Next, a gel mixture (NuSil 8100 + 0.15% Sylgard 184 cross-linking agent) is spin-coated on top of the membrane-on-plate, which is mounted on a spin coater (Laurell WS-650Mz-23, Laurell Technologies, USA). Three to 4 ml of uncured gel mixture is added to and spun at 500 rpm/s for 50 s. The gel/membrane/plate composite is cured at 90°C for 8 hours. This protocol produces a PDMS layer of approximately ~50 μm. This process is then repeated a second time to build up the layer to ~100 μm. (iv) To form the top layer bearing fluorescent beads, ~10 ml of the uncured gel mixture is mixed with 800 μl of stock solution of custom-made fluorescent beads to create a gel + bead mixture, which is added to the top surface and spin-coated at 2500 rpm/s for 1 min to achieve a thin, ~1-μm bead layer. The bead layer is cured at 90°C for 8 hours. The density of beads is shown in fig. S9. The PDMS layer is also sticky, enabling the sample surface to be adhered to the composite (see the "Adhesion of a sample to the membrane composite" section).

Stiffness of the membrane composite and PDMS gels determined by uniaxial stretch

The stiffnesses of the composite membrane and porous/nonporous PDMS gels were measured using the uniaxial stretch device following the protocol previously established (*47*). Briefly, membrane and PDMS samples of 3 to 9 mm in width and 10 to 15 mm in length were prepared using a blade. The thickness was measured by finding the distance between fluorescent beads deposited on the top and bottom surfaces of each membrane using an inverted confocal microscope (Olympus FV3000). The sample was assembled with 3D-printed clips to avoid slippage. One clip was fixed, and the other was connected to a dual-mode lever arm system (model 300B, Aurora Scientific, Ontario, Canada), which can simultaneously serve both as a displacement generator and a force sensor. The sample was stretched uniaxially with a 0.005-Hz triangle signal generated by a computer. The output force and displacement signals were converted to stress and strain by normalizing with the cross area and initial length, respectively. The slope of a regression between stress and strain between 0 and 20% strain provided an estimate of the Young's modulus (fig. S10). The Young's modulus of two composites was measured.

Measurements of sample stiffness

The center of the composite membrane was marked by depositing a droplet of 1-μm fluorescent bead solution (AFP-0865-2, Spherotech, IL, USA) on the bottom. First, images of beads embedded on the top surface were acquired near the center of the membrane before and after the composite membrane was stretched through rotation of a fixture shown in fig. S3, which resulted in a vertical displacement. After placing a sample near the center on the membrane, images were acquired before and after applying the prescribed stretch. Image sets with and without a sample were acquired within ~1.5-mm distance between each other. Each stretched image was acquired within ~2 min after applying the stretch. Stretch experiments were performed ~20 min apart. To compute the global strain ε^{o}_{rr} or local strain ε_{rr}, strains were averaged over the entire field of view. Stiffness was estimated using Eq. 2 and Fig. 1C. Each membrane was repeatedly used until the surface beads deteriorated during multiple sample measurements.

Imaging and strain mapping

All imaging experiments were conducted on an inverted confocal microscope (Olympus, FV3000) and a widefield scope (Olympus, ix83). Local displacements were quantified by applying particle imaging velocimetry (PIV) to the stretched image of beads and a reference image (*48*). The cross-correlation window size was chosen to be 32 × 32 pixels, and the window overlap was 28 pixels. To improve the accuracy of PIV in determining beads displacements, the stretched image was first shrunk by a factor of 12 to 13% before performing PIV. After performing PIV on the shrunk image, the image shrinkage factor was further adjusted until the average displacement measured from each PIV analysis became smaller than 3 pixels. Since both the PDMS and the membrane are optically clear, no special considerations were needed to account for a loss of optical clarity in fluorescent bead imaging through the composite membrane from below.

Agarose preparation

Blocks of agarose samples with 1.5, 2.0, and 2.5% concentration were prepared by adding low-melting-point agarose (A9414, Sigma-Aldrich) to warm HBSS (Corning Life Sciences, Tewksbury, MA) and cooling. Slices with 12 mm in diameter and 300 to 600 μm in thickness were prepared using a custom-built aluminum cylinder and a blade.

Porous PDMS

Porous PDMS samples were prepared using previously established protocols (*49*, *50*). Briefly, a soft PDMS elastomeric gel solution (see the "Preparation of a composite membrane" section) was mixed with a template solution for pores (ethanol: H_2O = 2:1) at the final volume ratio of PDMS:template solution = 10:2. The mixture solution was stirred using a magnetic stirrer at ~300 rpm while kept at ~80°C for ~20 min until pores were trapped. The mixture was then cured in an oven at ~65°C for 1 hour. As for the control nonporous PDMS, we fabricated PDMS samples in the same manner using the PDMS solution alone. Lastly, samples were cut into discs of 6.5 mm in radius and 2 to 2.5 mm in thickness and measured as described in Fig. 1.

Mouse lung slice preparation

Frozen mouse lung slices (C57BL/6J, 8 to 10 weeks old, three mice) were obtained as a gift from X. Ai and Y. Bai at Massachusetts General Hospital, Boston. These slices were prepared and frozen as per established procedures (*16*) approved by the Institutional Animal Care and Use Committee at Massachusetts General

Hospital. Briefly, excised mouse lungs were insufflated with 1.5% low-melting-point agarose in HBSS (Corning Life Sciences, Tewksbury, MA), cooled, and then sectioned into 150-μm-thick slices (VF-300; Precisionary Instruments, Greenville, NC). The slices were incubated overnight at 37°C in 1:1 Dulbecco's modified Eagle's medium (DMEM)/F-12 supplemented with penicillin, streptomycin, kanamycin, and amphotericin B (Invitrogen, Cambridge, MA), transferred to cryovials comprising a cryopreservation medium of 10% dimethyl sulfoxide diluted in DMEM/F-12 medium, and stored in liquid nitrogen. On the day of the experiment, the frozen cryovial was thawed rapidly in a 37°C water bath, and each slice was carefully removed and washed once in fresh culture medium before use.

Human lung slice preparation

Frozen human slices were purchased from the Institute for In Vitro Sciences (IIVS) Inc., Gaithersburg, MD. Normal (nondiseased) slices were obtained from a donor (procured through Novabiosis, Durham, NC) who was a 59-year-old female subject without any history of lung-related diseases. Emphysematous slices were obtained from a donor (procured through International Institute for the Advancement of Medicine, Edison, NJ) who was a 66-year-old male subject with a history of COPD that is often accompanied emphysema causing parenchymal destruction. Lung slices were prepared and frozen according to established procedures outlined in IIVS's recent publication (*51*). Briefly, the donor lung meeting the desired disease status was received on ice, had overt quality confirmed, and was filled with an isotonic 0.8% low melting point (Molecular Biology Grade) agarose (Bioworld, Dublin, OH; CAS# 9012-36-6) in HBSS and DMEM/F-12 (1:1 ratio) buffer also containing antibiotic/antimycotic. After storage on ice to allow the agarose to gel, the lung lobes are sectioned into ~1.5-cm-thick tissue blocks, cored into 8-mm-diameter cylinders, and sliced to approximately 500 ± 100 μm mean thickness using a Krumdieck MD4000 slicer before cryopreservation.

Adhesion of a sample to the membrane composite

The agarose sample or PCLS was placed upon the membrane composite and lightly air-dried with an airflow at a 2 psi (~14 kPa) pressure imposed for 1 min from a tube of 4-mm inner diameter held 3.5 cm above the slice, as previously described (*26*). This ensured prompt adhesion between the sample surface and the composite. To validate the adhesion of PCLS samples to the membrane composite, we imaged the parenchymal structure of a mPCLS through a phase-contrast channel and, simultaneously, imaged beads through a fluorescence channel on an inverted widefield scope (Olympus, ix83) (fig. S19). The means of average in-plane strain, $(\varepsilon_{xx} + \varepsilon_{yy})/2$, computed from structure (13.31%; fig. S19C) and beads (13.33%; fig. S19E), were identical, confirming that the PCLS and the substrate were stretched without slip.

Autocorrelation analysis for spatial structure

The spatial correlations of the strain maps and the autofluorescent images were estimated by computing the spatial autocorrelation function (*20*)

$$C(r) = \frac{1}{N\ \mathrm{var}(\overline{q})} \sum_{i,j=1}^{N} \left[\sum_{|r_i - r_j| = r} \delta\overline{q_i} \delta\overline{q_j} \right] \tag{3}$$

where q is the signal of interest (strain or autofluorescence), $\delta\overline{q_i}$ is the circularly averaged local departure of q at position r_i from its spatial mean $\overline{q}$, $\mathrm{var}(\overline{q})$ is the variance of q, and $|r_i - r_j| = r$ denotes equality within a uniform bin width of 10 μm, within which there are N points. The characteristic length ρ of the autocorrelation was calculated as a distance at which C decreased to 0.5. The decay of $C(r)$ indicates the length scale of spatial heterogeneity. For example, if the heterogeneity in an image is correlated over larger distances, then $C(r)$ will decay slower toward larger distances, and hence, ρ will be larger.

Alveolar area distributions

Alveolar areas were used as a metric to quantify structure, and datasets for alveolar areas from both emphysematous and non-emphysematous tissue samples were collected via manual alveolar tracing from fluorescent images. A chi-square test failed to reject the null hypothesis that these distributions were fit by a lognormal distribution at $P < 0.05$. A best-fit lognormal distribution was used to describe the area datasets.

Creation of network models

Next, these area distributions were converted into spring networks that matched the experimental distributions. To accomplish this, first the alveolar area probability distribution from a healthy tissue was used to create a population of "input circles" having the same distribution. The circles were arranged randomly in 2D and then densely packed. Each healthy network had approximately 980 input circles, and the networks as a whole were round and approximately 7 mm in diameter, similar to the hPCLSs. This size was chosen to have a sufficiently large number of alveoli while limiting the amount of time and computation necessary to create the networks. These densely packed input circles were converted into polygons with edges that are the springs in the network model.

Between sets of three circles, there is an area that represents a septal junction, and it was found that a node placed at a point within the triangle weighted by the inverse of the areas of the input circles that made that triangle well-maintained the structure of the densely packed circle diagram, similar to a Voronoi diagram. These nodes were then connected by edges that connect adjacent triangles, and these edges became the springs of the network with each representing a slab of tissue. Once this modified Voronoi diagram was made, the input circles were discarded. These polygons bordered by springs that represent alveoli are referred to as "cells" (fig. S11).

Once a nascent spring network was created, the parameters of the springs were established as follows. This model used linear springs, due to the low strain values, with their spring constants k_s linked to the Young's modulus Y of the septal wall as follows

$$k_s = \frac{Yhw}{L_0} \tag{4}$$

where h and w are the height and width of the slab, and L_0 is the resting length of the spring. Since the initial state of the spring

network is not at equilibrium, the nodes on the border of the network were fixed, and the internal node positions were moved iteratively until the total elastic energy was minimized. Once this was accomplished, an initial spring network was created.

Matching the network with sample structure

The initial networks created as described above had cell area distributions that were slightly larger than the input alveolar area distributions. Hence, the networks were scaled down by the mean ratio of the radii of the experimental data and the cells of the network. However, there still remained some difference between the experimental and network area distributions. Further correction was accomplished by iteratively modifying the springs to change the areas and structure of the network. For this correction, physiological units of the springs are not necessary. Hence, the *Ywh* term in Eq. 4 was set to 1, and the resting length of the springs was set to 20% the Vononoi diagram edge length of that spring. This provides heterogeneity in spring constant and simulates a prestress such that if a spring is softened, then the network will be out of equilibrium.

To match the area distribution of the network to the desired best-fit distribution of the data, a method was developed called "Probability Density Function Matching" (PDF Matching) (fig. S12). For this process, the area distribution of cells in the network and the desired area distribution of alveolar areas in the samples were discretized and normalized, and the sample PDF was subtracted from the network PDF. Where the greatest difference between the two distributions occurred, a random cell from the network from that discretized bin was selected. A random spring from that cell was elongated by 20%, the corresponding stiffness was changed to reflect the spring length using Eq. 4, and then the entire spring network was solved for equilibrium. This causes the selected cell to increase in area and the cells around that cell to decrease in area, effectively flattening the area distribution at that location and reducing the difference between the distributions. This process was repeated iteratively until the coefficient of determination between the input distribution and the network distribution was >0.99, indicating that the two PDFs matched well. Once this threshold was reached, the spring network was deemed statistically equivalent to the healthy hPCLS samples. This provided the healthy network.

A similar PDF matching approach was applied to the healthy network to convert it into an emphysematous network. The emphysematous sample area PDF was subtracted from the healthy network area PDF, and where the greatest difference between the distributions occurred, a random cell from that bin was chosen, and a random spring from that cell was cut. This spring cutting reflects the experimental finding that septal walls rupture in emphysema (*33*). The cells adjoined by the cut spring were then merged. This was repeated iteratively until the network area distribution matched the emphysematous area distribution. Once the iterations were completed, the network was considered the emphysematous network. This process of converting the healthy network into an emphysematous network was chosen rather than creating a new emphysematous network from the sample distribution, in part due to being substantially faster but also so a direct network-to-network analysis of the number of cut springs to convert from a healthy network to an emphysematous network could be obtained. After the healthy and emphysematous networks were created, the resting lengths of the springs were set to their apparent length within the network such that the entire network was at equilibrium. This was done to represent the network at its initial prestress and to eliminate discrepancies caused between networks during PDF matching. At this stage, the network configuration represents the structure of the tissue in personalized spring network form. From this process, two corresponding networks were produced, one healthy and one emphysematous.

Model parameters

For the networks to behave as the tissue they represent, it is necessary to define the mechanical properties of the springs in physiological units. To establish the material properties of the septal springs, the geometry of the alveolar septum was used to determine the stiffness of the springs. For this, Eq. 4 was used again; however, the cross-sectional area was determined by the height of the hPCLS sample and the mean width of the alveolar septal walls. Although the height terms cancel out, they were included for clarity.

To estimate the width of the alveolar walls, histological images were taken of the tissue after fixation. These images were skeletonized such that a center line for the walls was created, and then the distance from this center line to the edge of the tissue was measured for each pixel in the skeleton (fig. S13), creating a distribution of thicknesses for the network. Nonwall areas were manually removed from the images to prevent overestimation of the septal wall thicknesses. To perform this analysis, on the basis of the outline of IPSDK SMART Segmentation Machine Learning algorithm (Reactiv'IP, France), we developed our own algorithm in MATLAB.

The effect of tissue fixation on wall thickness was evaluated by comparing the alveolar areas between fluorescent images and histological images. Alveolar area distributions from the histological images were collected through manual tracing. Although the areas from the histological images also fit a lognormal distribution, the fixation caused the tissue to shrink. On the basis of conservation of mass, this would cause the walls to thicken. To correct this, a Bayesian analysis was used to compare a scaled version of the area distribution from fluorescent images to the histological area distribution. The scaling multiplier that maximized the Bayes factor, the ratio of the probability of the null hypothesis to that of the alternative hypothesis (fig. S14), was used to calculate the linear strain on the septal walls due to sample shrinkage. The corresponding transverse strain was determined using a Poisson's ratio of 0.5 for the wall tissue, which was used to correct the wall thickness due to fixation.

Calculating the network modulus

Once the networks were created and the physiological units of the springs were defined, the networks were mechanically stretched in silico to determine their mechanical properties as follows. The total strain energy E_{net} of the network is given by

$$E_{net} = \frac{1}{2} Y_{net} \epsilon^2 V_{net} \tag{5}$$

where Y_{net} is the Young's modulus of the network, ϵ is the linear radial strain on the network, and V_{net} is the initial volume, defined by the area of the network multiplied by h, the sample thickness. Thus, Y_{net} can be obtained by taking the second derivative of the strain energy density. The strain energy can also be calculated by summing the energy of all the linear springs within the network,

using the following relation

$$E_{\text{net}} = \sum_{i=1}^{n} \frac{1}{2} k_i \Delta x_i^2 \quad (6)$$

where n is the number of springs in the network, k_i is the spring constant of spring i, calculated with Eq. 5, and Δx_i is the extension of spring i. To find this relation between energy and strain, the network was stretched equi-biaxially to a set of strains up to 0.05, the network was solved at each strain, and the strain energy was calculated. The resulting energy-strain plot was fit with a second-order equation. The second derivative of this equation divided by the sample volume was then used as an estimate of the Young's modulus of the whole network.

With a known input wall modulus and a measured output network modulus for a given network configuration, it is possible to find the relation between the two moduli. The ratio of the input modulus to the output modulus was constant for all input moduli. This means that once the relation between the input wall modulus and the output network modulus is known, the measured Young's modulus from the hPCLS samples can be used to back-calculate the corresponding Young's modulus of the alveolar septal wall of that sample. For this reason, the Young's modulus of all the springs was set to 1, so the ratio of input septal modulus and output network modulus could be calculated directly.

Hematoxylin and eosin staining

hPCLS (normal, $n = 6$; emphysematous, $n = 4$) were fixed in neutral buffered formalin. Seven-micrometer paraffin-embedded sections were processed for routine histological analyses using hematoxylin and eosin staining according to the manufacturer's instructions (Hematoxylin and Eosin Stain Kit, Vector Laboratories).

Protein profiling by silver staining

hPCLSs (normal, $n = 6$; COPD, $n = 4$) were homogenized in the presence of protease inhibitors (Thermo Scientific Halt Protease and Phosphatase Inhibitor Cocktail, Thermo Fisher Scientific). Bichinchoninic acid assay (BCA) protein assay (Bio-Rad) was used for measuring total protein concentration. Equal amounts of protein (~6 μg) were separated by polyacrylamide gel electrophoresis, and gels were silver-stained by a Silver Stain Plus kit (Bio-Rad).

Enzyme profiling

Proteome profiler array was performed using the Human Protease Array Kit (R&D Systems Inc.) according to the manufacturer's instructions. Samples were homogenized (normal, $n = 6$; emphysematous, $n = 4$) and after the BCA protein assay (Bio-Rad). Equal amounts (150 μg) of total protein were used for each array membrane containing 35 enzymes. The array dot containing films were scanned and analyzed in ImageJ using the "gels" plugin. The details of the intensity profiles are given in fig. S17.

Statistical analysis

The healthy and emphysematous hPCLS stiffness values were compared using unpaired Student's one-way t test because stiffness was expected to be smaller in emphysema. These analyses were carried out in SigmaPlot (Palo Alto, CA, USA). Significance was accepted for $P < 0.05$. Distributions and lognormal fits were done in MATLAB R2021a (MathWorks, MA, USA). Bayesian t test was done in JASP 0.16 (University of Amsterdam). Posterior distributions were calculated in MATLAB using a custom code that assumed unknown mean and variance in the form of a two-parameter gamma-normal distribution and a normal distribution for the likelihood function. To avoid bias, nearly uniform prior distributions were used in the calculations.

Supplementary Materials

This PDF file includes:

Supplementary Text
Figs. S1 to S19

View/request a protocol for this paper from *Bio-protocol*.

REFERENCES AND NOTES

1. D. Stolz, T. Mkorombindo, D. M. Schumann, A. Agusti, S. Y. Ash, M. Bafadhel, C. Bai, J. D. Chalmers, G. J. Criner, S. C. Dharmage, F. M. E. Franssen, U. Frey, M. Han, N. N. Hansel, N. M. Hawkins, R. Kalhan, M. Konigshoff, F. W. Ko, T. M. Parekh, P. Powell, M. Rutten-van Molken, J. Simpson, D. D. Sin, Y. Song, B. Suki, T. Troosters, G. R. Washko, T. Welte, M. T. Dransfield, Towards the elimination of chronic obstructive pulmonary disease: A Lancet Commission. *Lancet* **400**, 921–972 (2022).
2. B. Suki, J. H. T. Bates, E. Bartolak-Suki, Remodeling of the aged and emphysematous lungs: Roles of microenvironmental cues. *Compr. Physiol.* **12**, 3559–3574 (2022).
3. E. C. Lucey, R. H. Goldstein, P. J. Stone, G. L. Snider, Remodeling of alveolar walls after elastase treatment of hamsters. Results of elastin and collagen mRNA in situ hybridization. *Am. J. Respir. Crit. Care Med.* **158**, 555–564 (1998).
4. G. Vlahovic, M. L. Russell, R. R. Mercer, J. D. Crapo, Cellular and connective tissue changes in alveolar septal walls in emphysema. *Am. J. Respir. Crit. Care Med.* **160**, 2086–2092 (1999).
5. I. A. Greaves, H. J. Colebatch, Elastic behavior and structure of normal and emphysematous lungs post mortem. *Am. Rev. Respir. Dis.* **121**, 127–136 (1980).
6. J. H. Bates, C. G. Irvin, R. Farre, Z. Hantos, Oscillation mechanics of the respiratory system. *Compr. Physiol.* **1**, 1233–1272 (2011).
7. R. S. Harris, Pressure-volume curves of the respiratory system. *Respir. Care* **50**, 78–98; discussion 98-79 (2005).
8. M. A. Hajji, T. A. Wilson, S. J. Lai-Fook, Improved measurements of shear modulus and pleural membrane tension of the lung. *J. Appl. Physiol. Respir. Environ. Exerc. Physiol.* **47**, 175–181 (1979).
9. B. Suki, D. Stamenovic, R. D. Hubmayr, Lung Parenchymal Mechanics, in *Comprehensive Physiology, The Respiratory System, Respiration Mechanics: Organ, Cell, Molecule*, J. J. Fredberg, G. C. Sieck, W. T. Gerthoffer, Eds. (Wiley-Blackwell, 2011), vol. 1, pp. 1317–1351.
10. A. Marinkovic, F. Liu, D. J. Tschumperlin, Matrices of physiologic stiffness potently inactivate idiopathic pulmonary fibrosis fibroblasts. *Am. J. Respir. Cell Mol. Biol.* **48**, 422–430 (2013).
11. I. Jorba, G. Beltran, B. Falcones, B. Suki, R. Farre, J. M. Garcia-Aznar, D. Navajas, Nonlinear elasticity of the lung extracellular microenvironment is regulated by macroscale tissue strain. *Acta Biomater.* **92**, 265–276 (2019).
12. S. Bou Jawde, A. Takahashi, J. H. T. Bates, B. Suki, An analytical model for estimating alveolar wall elastic moduli from lung tissue uniaxial stress-strain curves. *Front. Physiol.* **11**, 121 (2020).
13. L. Bin, Y. Ronghua, Y. Peng, M. Awad, M. Choti, R. Taylor, paper presented at the Proceedings of the IEEE 32nd Annual Northeast Bioengineering Conference, Easton, PA, USA, 01 to 02 April 2006, p. 81–82 .
14. K. D. Costa, M. M. Y. Ho, C. T. Hung, Multi-Scale Measurement of Mechanical Properties of Soft Samples with Atomic Force Microscopy, paper presented at: Summer Bioengineering Conference, Sonesta Beach Resort in Key Biscayne, Florida, 25 to 29 June 2003, p. 0285–0286.
15. S. Park, C. T. Duong, J. H. Lee, S. S. Lee, K. Son, Effect of tip geometry of atomic force microscope on mechanical responses of bovine articular cartilage and agarose gel. *Int. J. Precis. Eng. Manuf.* **11**, 129–136 (2010).
16. S. R. Rosner, S. Ram-Mohan, J. R. Paez-Cortez, T. L. Lavoie, M. L. Dowell, L. Yuan, X. Ai, A. Fine, W. C. Aird, J. Solway, J. J. Fredberg, R. Krishnan, Airway contractility in the precision-cut lung slice after cryopreservation. *Am. J. Respir. Cell Mol. Biol.* **50**, 876–881 (2014).
17. C. G. Irvin, J. H. Bates, Measuring the lung function in the mouse: The challenge of size. *Respir. Res.* **4**, 4 (2003).

18. S. Chang, N. Kwon, J. Kim, Y. Kohmura, T. Ishikawa, C. K. Rhee, J. H. Je, A. Tsuda, Synchrotron X-ray imaging of pulmonary alveoli in respiration in live intact mice. *Sci. Rep.* **5**, 8760 (2015).
19. H. Parameswaran, E. Bartolak-Suki, H. Hamakawa, A. Majumdar, P. G. Allen, B. Suki, Three-dimensional measurement of alveolar airspace volumes in normal and emphysematous lungs using micro-CT. *J. Appl. Physiol.* **107**, 583–592 (2009).
20. J. A. Park, J. H. Kim, D. Bi, J. A. Mitchel, N. T. Qazvini, K. Tantisira, C. Y. Park, M. McGill, S. H. Kim, B. Gweon, J. Notbohm, R. Steward Jr., S. Burger, S. H. Randell, A. T. Kho, D. T. Tambe, C. Hardin, S. A. Shore, E. Israel, D. A. Weitz, D. J. Tschumperlin, E. P. Henske, S. T. Weiss, M. L. Manning, J. P. Butler, J. M. Drazen, J. J. Fredberg, Unjamming and cell shape in the asthmatic airway epithelium. *Nat. Mater.* **14**, 1040–1048 (2015).
21. M. Ochs, J. R. Nyengaard, A. Jung, L. Knudsen, M. Voigt, T. Wahlers, J. Richter, H. J. Gundersen, The number of alveoli in the human lung. *Am. J. Respir. Crit. Care Med.* **169**, 120–124 (2004).
22. H. D. Held, C. Martin, S. Uhlig, Characterization of airway and vascular responses in murine lungs. *Br. J. Pharmacol.* **126**, 1191–1199 (1999).
23. F. Meng, N. H. Wu, A. Nerlich, G. Herrler, P. Valentin-Weigand, M. Seitz, Dynamic virus-bacterium interactions in a porcine precision-cut lung slice coinfection model: Swine influenza virus paves the way for Streptococcus suis infection in a two-step process. *Infect. Immun.* **83**, 2806–2815 (2015).
24. V. Neuhaus, K. Schwarz, A. Klee, S. Seehase, C. Forster, O. Pfennig, D. Jonigk, H. G. Fieguth, W. Koch, G. Warnecke, V. Yusibov, K. Sewald, A. Braun, Functional testing of an inhalable nanoparticle based influenza vaccine using a human precision cut lung slice technique. *PLOS ONE* **8**, e71728 (2013).
25. Y. Bai, N. Krishnamoorthy, K. R. Patel, I. Rosas, M. J. Sanderson, X. Ai, Cryopreserved human precision-cut lung slices as a bioassay for live tissue banking. A viability study of bronchodilation with bitter-taste receptor agonists. *Am. J. Respir. Cell Mol. Biol.* **54**, 656–663 (2016).
26. S. Ram-Mohan, Y. Bai, N. Schaible, A. J. Ehrlicher, D. P. Cook, B. Suki, D. A. Stoltz, J. Solway, X. Ai, R. Krishnan, Tissue traction microscopy to quantify muscle contraction within precision-cut lung slices. *Am. J. Physiol. Lung Cell. Mol. Physiol.* **318**, L323–L330 (2020).
27. C. Dassow, L. Wiechert, C. Martin, S. Schumann, G. Muller-Newen, O. Pack, J. Guttmann, W. A. Wall, S. Uhlig, Biaxial distension of precision-cut lung slices. *J. Appl. Physiol.* **108**, 713–721 (2010).
28. T. L. Lavoie, R. Krishnan, H. R. Siegel, E. D. Maston, J. J. Fredberg, J. Solway, M. L. Dowell, Dilatation of the constricted human airway by tidal expansion of lung parenchyma. *Am. J. Respir. Crit. Care Med.* **186**, 225–232 (2012).
29. N. Davidovich, J. Huang, S. S. Margulies, Reproducible uniform equibiaxial stretch of precision-cut lung slices. *Am. J. Physiol. Lung Cell. Mol. Physiol.* **304**, L210–L220 (2013).
30. J. R. Mondonedo, E. Bartolak-Suki, S. Bou Jawde, K. Nelson, K. Cao, A. Sonnenberg, W. P. Obrochta, J. Imsirovic, S. Ram-Mohan, R. Krishnan, B. Suki, A high-throughput system for cyclic stretching of precision-cut lung slices during acute cigarette smoke extract exposure. *Front. Physiol.* **11**, 566 (2020).
31. M. Schleputz, S. Uhlig, C. Martin, Electric field stimulation of precision-cut lung slices. *J. Appl. Physiol.* **110**, 545–554 (2011).
32. M. Schleputz, A. D. Rieg, S. Seehase, J. Spillner, A. Perez-Bouza, T. Braunschweig, T. Schroeder, M. Bernau, V. Lambermont, C. Schlumbohm, K. Sewald, R. Autschbach, A. Braun, B. W. Kramer, S. Uhlig, C. Martin, Neurally mediated airway constriction in human and other species: A comparative study using precision-cut lung slices (PCLS). *PLOS ONE* **7**, e47344 (2012).
33. S. Kononov, K. Brewer, H. Sakai, F. S. Cavalcante, C. R. Sabayanagam, E. P. Ingenito, B. Suki, Roles of mechanical forces and collagen failure in the development of elastase-induced emphysema. *Am. J. Respir. Crit. Care Med.* **164**, 1920–1926 (2001).
34. A. Sharafkhaneh, N. A. Hanania, V. Kim, Pathogenesis of emphysema: From the bench to the bedside. *Proc. Am. Thorac. Soc.* **5**, 475–477 (2008).
35. S. Ito, E. P. Ingenito, K. K. Brewer, L. D. Black, H. Parameswaran, K. R. Lutchen, B. Suki, Mechanics, nonlinearity, and failure strength of lung tissue in a mouse model of emphysema: Possible role of collagen remodeling. *J. Appl. Physiol.* **98**, 503–511 (2005).
36. F. Polverino, J. Rojas-Quintero, X. Wang, H. Petersen, L. Zhang, X. Gai, A. Higham, D. Zhang, K. Gupta, A. Rout, I. Yambayev, V. Pinto-Plata, L. M. Sholl, D. Cunoosamy, B. R. Celli, J. Goldring, D. Singh, Y. Tesfaigzi, J. Wedzicha, H. Olsson, C. A. Owen, A disintegrin and metalloproteinase domain-8: A novel protective proteinase in chronic obstructive pulmonary disease. *Am. J. Respir. Crit. Care Med.* **198**, 1254–1267 (2018).
37. L. Cui, H. Li, M. Xie, X. Xu, Y. Zhang, W. Wang, S. Dou, W. Xiao, Relationship between proteinase with a disintegrin and a metalloproteinase domain-9 (ADAM9), inflammation, airway remodeling, and emphysema in COPD patients. *Int. J. Chron. Obstruct. Pulmon. Dis.* **Volume 15**, 3335–3346 (2020).
38. M. L. Padilla, N. I. Galicki, J. Kleinerman, M. Orlowski, M. Lesser, High cathepsin B activity in alveolar macrophages occurs with elastase-induced emphysema but not with bleomycin-induced pulmonary fibrosis in hamsters. *Am. J. Pathol.* **131**, 92–101 (1988).
39. X. Zhang, P. Shan, R. Homer, Y. Zhang, I. Petrache, P. Mannam, P. J. Lee, Cathepsin E promotes pulmonary emphysema via mitochondrial fission. *Am. J. Pathol.* **184**, 2730–2741 (2014).
40. H. Takahashi, K. Ishidoh, D. Muno, A. Ohwada, T. Nukiwa, E. Kominami, S. Kira, Cathepsin L activity is increased in alveolar macrophages and bronchoalveolar lavage fluid of smokers. *Am. Rev. Respir. Dis.* **147**, 1562–1568 (1993).
41. P. M. Andrault, A. C. Schamberger, T. Chazeirat, D. Sizaret, J. Renault, C. A. Staab-Weijnitz, E. Hennen, A. Petit-Courty, M. Wartenberg, A. Saidi, T. Baranek, S. Guyetant, Y. Courty, O. Eickelberg, G. Lalmanach, F. Lecaille, Cigarette smoke induces overexpression of active human cathepsin S in lungs from current smokers with or without COPD. *Am. J. Physiol. Lung Cell. Mol. Physiol.* **317**, L625–L638 (2019).
42. K. Imai, S. S. Dalal, E. S. Chen, R. Downey, L. L. Schulman, M. Ginsburg, J. D'Armiento, Human collagenase (matrix metalloproteinase-1) expression in the lungs of patients with emphysema. *Am. J. Respir. Crit. Care Med.* **163**, 786–791 (2001).
43. K. Ohnishi, M. Takagi, Y. Kurokawa, S. Satomi, Y. T. Konttinen, Matrix metalloproteinase-mediated extracellular matrix protein degradation in human pulmonary emphysema. *Lab. Invest.* **78**, 1077–1087 (1998).
44. S. Braber, P. J. Koelink, P. A. Henricks, P. L. Jackson, F. P. Nijkamp, J. Garssen, A. D. Kraneveld, J. E. Blalock, G. Folkerts, Cigarette smoke-induced lung emphysema in mice is associated with prolyl endopeptidase, an enzyme involved in collagen breakdown. *Am. J. Physiol. Lung Cell. Mol. Physiol.* **300**, L255–L265 (2011).
45. H. Yoshie, N. Koushki, R. Kaviani, M. Tabatabaei, K. Rajendran, Q. Dang, A. Husain, S. Yao, C. Li, J. K. Sullivan, M. Saint-Geniez, R. Krishnan, A. J. Ehrlicher, Traction force screening enabled by compliant PDMS elastomers. *Biophys. J.* **114**, 2194–2199 (2018).
46. S. M. Klein, V. N. Manoharan, D. J. Pine, F. F. Lange, Preparation of monodisperse PMMA microspheres in nonpolar solvents by dispersion polymerization with a macromonomeric stabilizer. *Colloid Polym. Sci.* **282**, 7–13 (2003).
47. F. S. A. Cavalcante, S. Ito, K. Brewer, H. Sakai, A. M. Alencar, M. P. Almeida, J. S. Andrade Jr., A. Majumdar, E. P. Ingenito, B. Suki, Mechanical interactions between collagen and proteoglycans: Implications for the stability of lung tissue. *J. Appl. Physiol.* **98**, 672–679 (2005).
48. J. H. Kim, X. Serra-Picamal, D. T. Tambe, E. H. Zhou, C. Y. Park, M. Sadati, J. A. Park, R. Krishnan, B. Gweon, E. Millet, J. P. Butler, X. Trepat, J. J. Fredberg, Propulsion and navigation within the advancing monolayer sheet. *Nat. Mater.* **12**, 856–863 (2013).
49. Y. Kwak, Y. Kang, W. Park, E. Jo, J. Kim, Fabrication of fine-pored polydimethylsiloxane using an isopropyl alcohol and water mixture for adjustable mechanical, optical, and thermal properties. *RSC Adv.* **11**, 18061–18067 (2021).
50. P. Thurgood, S. Baratchi, C. Szydzik, A. Mitchell, K. Khoshmanesh, Porous PDMS structures for the storage and release of aqueous solutions into fluidic environments. *Lab Chip* **17**, 2517–2527 (2017).
51. V. Patel, K. Amin, D. Allen, L. Ukishima, A. Wahab, C. Grodi, H. Behrsing, Comparison of long-term human precision-cut lung slice culture methodology and response to challenge: An argument for standardisation. *Altern. Lab. Anim.* **49**, 209–222 (2021).

Acknowledgments: PCLS from IIVS were generated by staff in the Respiratory Toxicology Program (V. Patel, L. Ukishima, A. Wahab, J. Alvarez, K. Battle, and M. Marimoutou). **Funding:** This work was supported by Boston University Micro and Nano Imaging Facility, National Institutes of Health S10OD024993, National Institutes of Health 1R41HL147673 (to B.S.), National Institutes of Health U01 HL139466 (to B.S.), and National Institutes of Health R21AI151695 (to R.K.). **Author contributions:** Conceptualization: J.H.K., R.K., and B.S. Methodology: J.H.K., N.S., J.K.H., E.B.-S., Y.D., J.H., A.S., H.P.B., R.K., and B.S. Investigation: J.H.K., N.S., J.K.H., E.B.S., Y.D., J.H., and A.S. Visualization: J.H.K., J.K.H., and B.S. Supervision: K.R.L., R.K., and B.S. Writing—original draft: J.H.K., J.K.H., R.K., and B.S. Writing—review and editing: J.H.K., K.R.L., R.K., and B.S. **Competing interests:** R.K. and B.S. are co-founders and equity holders of Mechanobiologix LLC. B.S., R.K., J.H.K., N.S., and J.K.H. are inventors on a patent application related to this work filed by Boston University and Beth Israel Deaconess Medical Center (no. 63/352,667, filed 16 June 2022, status: pending provisional application). The authors declare that they have no other competing interests. **Data and materials availability:** All data needed to evaluate the conclusions in the paper are present in the paper and/or the Supplementary Materials. The code that was used for analysis and modeling is available at Zenodo using the DOI 10.5281/zenodo.7820152.

Submitted 9 October 2022
Accepted 14 April 2023
Published 19 May 2023
10.1126/sciadv.adf2535